Postprint of: Burzyński S., Chróścielewski J., Daszkiewicz K., Witkowski W., Geometrically nonlinear FEM analysis of FGM shells based on neutral physical surface approach in 6-parameter shell theory, Composites Part B: Engineering, Vol. 107 (2016), pp. 203-213, DOI: 10.1016/j.compositesb.2016.09.015

Title: Geometrically nonlinear FEM analysis of FGM shells based on neutral physical surface approach in 6-parameter shell theory

Authors: Stanisław Burzyński, Jacek Chróścielewski, Karol Daszkiewicz, Wojciech Witkowski

Affiliation:
Gdańsk University of Technology, Faculty of Civil and Environmental Engineering,
Department of Mechanics of Materials and Structures,
80-233 Gdańsk, Narutowicza 11/12, Poland

Corresponding author:
Karol Daszkiewicz
Gdańsk University of Technology, Faculty of Civil and Environmental Engineering,
Department of Mechanics of Materials and Structures,
80-233 Gdańsk, Gabriela Narutowicza 11/12, Poland
Email: kardaszk@pg.edu.pl
Phone: +48 58 348 17 55

Abstract

The paper presents the formulation of the elastic constitutive law for functionally graded materials (FGM) on the grounds of nonlinear 6-parameter shell theory with the 6^{th} parameter being the drilling degree of freedom. The material law is derived by through-the-thickness integration of the Cosserat plane stress equations. The constitutive equations are formulated with respect to the neutral physical surface. The influence of the power-law exponent, micropolar characteristic length is evaluated in geometrically nonlinear FEM analyses. The results obtained with the neutral physical surface approach are compared with those computed with the middle surface approach. The influence of choice of the reference surface is observed especially in nonlinear stability analysis.

Keywords: A. Functionally graded materials (FGMs), B. buckling, C. Finite element analysis (FEA), neutral surface

1. Introduction

The functionally graded materials (FGMs) are characterized by continuous change of the constituent materials. They were introduced in Japan [1] at the end of XX century. The FGMs were proposed as new generation of laminated composites that are free from the material mismatches at interface surfaces of the laminate layers. In the case of shell structures the most popular is composition of metal and ceramic materials that gives the high stiffness and high heat-resistance. The volume fraction of the constituent materials, microstructure and material properties vary continuously in the thickness direction of the FGM section. The FGM shells may be applied in many branches of industry to optimize e.g. mechanical, thermal performance of structures.

The geometrically nonlinear analysis and postbuckling analysis of FGM shells have been performed analytically or numerically in many papers [2]. However, in majority of nonlinear studies only simply supported square plates [3,4], rectangular plates [5,6] or circular plates [7] have been analyzed. The geometrically nonlinear response of FGM shells with complex geometry have been investigated only in a limited number of papers. The results of nonlinear analysis for typical benchmark shell problems for the power law FGM section have been presented in [8] and for sigmoid FGM section in [9]. Recently, static analysis of FGM conical shells with the stress recovery was performed by Viola et al. [10], stability analysis of FGM sandwich plates by Fazzolari [11], the postbuckling analysis of square plate on an elastic foundation by Taczała et al. [12] and the nonlinear analysis of doubly curved panel resting on nonlinear elastic foundation by Tornabene and Reddy [13]. Natural frequencies of doubly-curved FGM shells were computed in [14–17] using different theoretical formulations. The influence of uniform and non-uniform temperature distribution [18], in-plane crack [19] and thermoelastic coupling [20] on the free vibrations of FGM plates was also investigated.

In [3–9] geometrically nonlinear computations with respect to the middle reference surface were performed. An alternative formulation based on the neutral physical surface was proposed for the first time for FGM section by Morimoto et al. [21]. Abrate [22] showed that

the neutral surface approach eliminates coupling between membrane and bending deformations in the linear analysis. Consequently, it is possible to describe the response of FGM shell using similar equations as of a homogenous shell. The comparison of results obtained under neutral and middle surface formulations has been presented for the circular and square plates in [23] and within the nonlinear analysis of skew plates in [24]. Prakash et al. [24] observed a bifurcation point on equilibrium paths only for the neutral physical surface approach. The results of linear analysis of beam and shell FGM structures modelled by 6-parameter shell element with drilling DOF have been presented in [25].

The present paper is concerned with formulation of FGM material on the grounds of nonlinear 6-parameter shell theory with the 6^{th} parameter (drilling) and its FEM implementation. We use C^0 4-node EANS finite element [26] with the combined enhanced assumed strain [27] and the assumed natural strain [28]. These two approaches have been shown in [26] to be an efficient remedy for the locking effect. Recently however, another ways of formulating robust shell finite elements were presented in [29–31].

Theoretical bases of the employed shell theory are to be found in the works of Reissner [32], Libai and Simmonds [33], cf. also [34–38] for some new aspects. As key characteristics of the theory we stress that it is statically and kinematically exact i.e.:

- 2D equilibrium equations of the shell-like body are obtained in the course of direct and exact through-the-thickness integration of 3D balance laws of linear and angular momentum of the Cauchy continuum,
- definitions of the 2D shell strain measures follow directly from an integral identity generated by the exact equilibrium equations.

Consequently, the kinematic model of the shell reference surface is formally equivalent to the Cosserat surface with three rigidly rotating directors. In derivation of the equations of motion only necessary mathematical requirements: continuity and appropriate smoothness of fields are taken into account without resorting to other assumptions typical for classical formulations.

Within such theoretical formulation the only local approximation appears when the constitutive relations are proposed. A brief account of what has been done so far in this field may be found in [39].

In this paper we formulate the elastic constitutive law for the functionally graded materials. As the starting point of the present paper we follow [40,41]. The material laws that incorporate a characteristic length of material have been derived by local through-the-thickness integration of the Cosserat plane stress (cf. for instance [42]). The constitutive relation is based on the following assumptions:

- membrane strains and in-plane curvatures are not symmetric,
- strains are small everywhere in the shell space,
- stress resultants and couple resultants are found from through-the-thickness integration of elastic Cosserat plane stress, making the assumption of the Reissner-Mindlin kinematics,
- the shell is sufficiently thin to assume that for every coordinate in the thickness direction the determinant μ of the shifter tensor $\mu_{\alpha\beta}$ satisfies the condition $\mu \approx 1$.

In comparison with the previous paper [43], here we formulate the constitutive equations of FGM on the neutral surface of the shell. In examples we examine the influence of the power-law exponent, micropolar material length and the choice of neutral or middle surface approach on the overall behavior of shells in FEM geometrically nonlinear analysis.

2. Governing equations

The equations of equilibrium and equations of motion, as well as strong and weak formulations for the present shell theory have been extensively studied in e.g. [26,39,44–46] and references given there. Therefore in this section only necessary aspects are discussed.

Let M denote the shell reference surface in the undeformed configuration (Fig. 1). As usual, the boundary ∂M is a union $\partial M = \partial M_d \cup \partial M_f$ where displacement and traction boundary conditions are imposed, respectively. It is assumed that M is smooth enough for

existence of the metric and curvature tensors. Typical point $\boldsymbol{x} \subset M$ is described by the pair $(\boldsymbol{x}, \boldsymbol{T}_0)$, where $\boldsymbol{x}$ is the position vector and $\boldsymbol{T}_0 \in SO(3)$ is the structure tensor composed of

$$\boldsymbol{t}_\beta^0 = \boldsymbol{x}_{,\beta}, \ \boldsymbol{t}^0 \equiv \boldsymbol{t}_3^0 = \frac{\boldsymbol{t}_1^0 \times \boldsymbol{t}_2^0}{\| \boldsymbol{t}_1^0 \times \boldsymbol{t}_2^0 \|}, \ \beta = 1,2, \ (.)_{,\beta} = \frac{\partial (.)}{\partial s^\beta} \tag{1}$$

The configuration space of the shell is defined as

$$U = C(M, g) = \left\{ \mathbf{u} = (\boldsymbol{u}, \boldsymbol{Q}) : M \to g = E^3 \times SO(3) \right\} \tag{2}$$

Here $\boldsymbol{Q}(\boldsymbol{x}) \in SO(3)$ is an independent proper orthogonal tensor. The space tangent to (2) at $\mathbf{u}$ is

$$W = T_{\mathbf{u}} U \cong C(M, g) = \left\{ \mathbf{w} : M \to g = E^3 \times so(3) \right\} \tag{3}$$

Due to the isomorphism $so(3) \cong E^3$ it is also true that

$$T_{\mathbf{u}} U \cong C(M, E) = \left\{ \mathbf{w} : M \to E = E^3 \times E^3 \right\} \tag{4}$$

As a result of deformation $\mathbf{u} = (\boldsymbol{u}, \boldsymbol{Q})$ the current position $\boldsymbol{y}(\boldsymbol{x})$ and the structure tensor $\boldsymbol{T}(\boldsymbol{x}) \in SO(3)$ (see Fig. 1) associated with the reference surface become

$$\boldsymbol{y}(\boldsymbol{x}) = \boldsymbol{x} + \boldsymbol{u}(\boldsymbol{x}), \quad \boldsymbol{t}_i(\boldsymbol{x}) = \boldsymbol{Q}(\boldsymbol{x}) \boldsymbol{t}_i^0(\boldsymbol{x}) = \boldsymbol{Q}(\boldsymbol{x}) \boldsymbol{T}_0(\boldsymbol{x}) \mathbf{e}_i = \boldsymbol{T}(\boldsymbol{x}) \mathbf{e}_i \tag{5}$$

In the present paper, we use the 4-node shell EANS element based on the modified Hu-Washizu principle, cf. also [44] and enhanced strain interpolation [26]. To minimize the membrane locking effect, in [26,44] the enhanced strain approach has been used to the only membrane strain components. The shear locking is treated with the help of the assumed natural strain [28].

In passing it is stressed that all the $SO(3)$-valued variables are interpolated using the multistep approach, as described in [44,46,47]. Various parametrization of $SO(3)$ are discussed in e.g. [48–50]. Here the canonical parametrization is used.

3. Constitutive relation

The FGM shell section with top ceramic surface (*c*) and bottom metal (*m*) surface is assumed, Fig. 2. The continuous change of volume fraction of ceramic V_c and metal V_m through the shell thickness is described by the power law

$$V_c = \left(\frac{z}{h} + \frac{1}{2}\right)^n, \quad V_m = 1 - V_c, \quad n \geq 0, \quad z \in [-\tfrac{1}{2}h, +\tfrac{1}{2}h] \tag{6}$$

where n is the power-law exponent and z is coordinate in the thickness direction (Fig. 2). Assumption of $n = 0$ gives the fully ceramic section and $n \to \infty$ the fully metal section.

The simple rule of mixture is used to calculate effective material properties $P(z)$ (e.g. elastic modulus E, shear modulus G) in the lamina of FGM

$$P(z) = P_c V_c + P_m V_m = (P_c - P_m)\left(\frac{z}{h} + \frac{1}{2}\right)^n + P_m \tag{7}$$

where P_c and P_m are the material properties of ceramic and metal constituents, respectively. The constant value of the Poisson ratio v is assumed, since the effect of its gradient on the results is negligible [5].

For FGM section we define the physical neutral surface as the surface where stresses and strains are zero. Based on this condition we calculate the shift z_0 of the physical neutral surface (Fig. 2) relative to the geometrical middle surface

$$z_0 = \frac{\int_{h^-}^{h^+} zE(z)dz}{\int_{h^-}^{h^+} E(z)dz} = \frac{h}{2}\frac{n(E_c - E_m)}{(n+2)(E_c + nE_m)} \tag{8}$$

where $h^+ = +\tfrac{1}{2}h$, $h^- = -\tfrac{1}{2}h$. The integrals in (8) are obtained in [43]. The maximal value of the shift $z_{0\max}$ may be determined by substitution $n_{\max} = \sqrt{\frac{2E_c}{E_m}}$ into (8)

$$z_{0\max} = \frac{h(E_c - E_m)}{2\left(\sqrt{E_c} + \sqrt{2E_m}\right)^2} \tag{9}$$

For homogenous isotropic section the shift equals zero. We assume the physical neutral surface as the reference surface in the subsequent calculations.

$$S_m = \int_{h^-}^{h^+} E(z)dz = \frac{E_c - E_m}{n+1}h + E_m h$$
$$S_b = \int_{h^-}^{h^+} (z - z_0)^2 E(z)dz = \frac{(E_m - E_c)h^3}{(n+1)(n+2)}\left[n\left(\frac{1}{2} - \frac{z_0}{h}\right)^2 + 2\left(\frac{z_0}{h}\right)^2 + \frac{1-n}{2(n+3)}\right] + E_c\frac{h^3}{12}\left(1 + 12\frac{z_0^2}{h^2}\right) \tag{10}$$

The integrals of elastic modulus (10) are derived to obtain information about membrane stiffness S_m and bending stiffness S_b of FGM section. Similar integration of shear modulus $G(z)$ gives $\bar{S}_m = \frac{S_m}{2(1+\nu)}$, $\bar{S}_b = \frac{S_b}{2(1+\nu)}$.

The following vectors of generalized strains $\mathbf{e}$ and stresses $\boldsymbol{\sigma}$ are defined at each lamina of the shell

$$\begin{aligned} \mathbf{e}^{\mathrm{T}} &= \left\{ \mathbf{e}_m \mid \mathbf{e}_d \right\} = \left\{ e_{11}\ e_{22}\ e_{12}\ e_{21} \mid \kappa_1\ \kappa_2 \right\} \\ \boldsymbol{\sigma}^{\mathrm{T}} &= \left\{ \boldsymbol{\sigma}_m \mid \boldsymbol{\sigma}_d \right\} = \left\{ \sigma_{11}\ \sigma_{22}\ \sigma_{12}\ \sigma_{21} \mid m_1\ m_2 \right\} \end{aligned} \tag{11}$$

Making the kinematical assumption of Reissner-Mindlin type we calculate the membrane components of the strain vector $\mathbf{e}_m$ from the following equation

$$\mathbf{e}_m = \boldsymbol{\varepsilon}_m + \left(z - z_0 \right) \boldsymbol{\varepsilon}_b \tag{12}$$

where $\boldsymbol{\varepsilon}_m$ and $\boldsymbol{\varepsilon}_b$ are the known strains at the shell reference surface

$$\boldsymbol{\varepsilon} = \{ \varepsilon_{11}\ \varepsilon_{22}\ \varepsilon_{12}\ \varepsilon_{21} | \varepsilon_1\ \varepsilon_2 \| \kappa_{11}\ \kappa_{22}\ \kappa_{12}\ \kappa_{21} | \kappa_1\ \kappa_2 \}^{\mathrm{T}} = \{ \boldsymbol{\varepsilon}_m | \boldsymbol{\varepsilon}_s \| \boldsymbol{\varepsilon}_b \mid \boldsymbol{\varepsilon}_d \}^{\mathrm{T}} \tag{13}$$

In (13) labels *m, s, b,* and *d* denote respectively: the membrane, shear, bending and drilling part. The first order shear deformation theory and higher-order shear theories give close results for analyzed thin FGM shells [51]. Additionally, in the shell space constant values of drilling strain components $\mathbf{e}_d = \boldsymbol{\varepsilon}_d$ are assumed, although some dependence between drilling couples and membrane strain components has been shown in [34].

The Cosserat plane stress formulation [41] is applied in each lamina of the shell section. The constitutive relation between vectors $\mathbf{e}$ and $\boldsymbol{\sigma}$ is described by the following matrix

$$\mathbf{C}^e = \left[\begin{array}{c:c} \mathbf{C}_{mm} & \mathbf{C}_{md} \\ \hdashline \mathbf{C}_{dm} & \mathbf{C}_{dd} \end{array} \right] = \left[\begin{array}{cccc:cc} Ea_1 & Ea_2 & 0 & 0 & 0 & 0 \\ Ea_2 & Ea_1 & 0 & 0 & 0 & 0 \\ 0 & 0 & G\mu_1 & G\mu_2 & 0 & 0 \\ 0 & 0 & G\mu_2 & G\mu_1 & 0 & 0 \\ \hdashline 0 & 0 & 0 & 0 & 2Gl^2 & 0 \\ 0 & 0 & 0 & 0 & 0 & 2Gl^2 \end{array} \right] \tag{14}$$

where $a_1 = \dfrac{1}{1-\nu^2}$, $a_2 = \nu a_1$, l is the micropolar characteristic length, $\mu_1 = \dfrac{1}{1-N^2}$, $\mu_2 = \dfrac{1-2N^2}{1-N^2}$ and N is the Cosserat coupling number, see e.g. [52]. Some experimental methods of micropolar parameters determination were reviewed in [53].

In comparison with our previous paper [43], here we formulate the FGM constitutive relation using the physical neutral surface approach. We assume that determinant μ of the shifter tensor $\mu_{\alpha\beta}$ equals 1. The membrane, bending and drilling stress resultants

$$\mathbf{s} = \{N^{11} N^{22} N^{12} N^{21} | Q^1 Q^2 \| M^{11} M^{22} M^{12} M^{21} | M^1 M^2\}^{\mathrm{T}} = \{\mathbf{s}_m | \mathbf{s}_s \| \mathbf{s}_b | \mathbf{s}_d\}^{\mathrm{T}} \tag{15}$$

are derived by integration of stresses through the shell thickness

$$\mathbf{s}_m = \int_{h^-}^{h^+} \boldsymbol{\sigma}_m \, dz = \int_{h^-}^{h^+} [\mathbf{C}_{mm}(\boldsymbol{\varepsilon}_m + (z - z_0)\boldsymbol{\varepsilon}_b) + \mathbf{C}_{md} \ \boldsymbol{\varepsilon}_d] \, dz = \int_{h^-}^{h^+} \mathbf{C}_{mm} \boldsymbol{\varepsilon}_m \ dz = S_m \mathbf{R} \boldsymbol{\varepsilon}_m \tag{16}$$

$$\begin{aligned} \mathbf{s}_b &= \int_{h^-}^{h^+} \boldsymbol{\sigma}_m (z - z_0) dz = \int_{h^-}^{h^+} [\mathbf{C}_{mm}[(z - z_0)\boldsymbol{\varepsilon}_m + (z - z_0)^2 \boldsymbol{\varepsilon}_b] + (z - z_0)\mathbf{C}_{md} \ \boldsymbol{\varepsilon}_d] \, dz \\ &= \int_{h^-}^{h^+} \mathbf{C}_{mm} (z - z_0)^2 \boldsymbol{\varepsilon}_b \ dz = S_b \mathbf{R} \boldsymbol{\varepsilon}_b \end{aligned} \tag{17}$$

$$\mathbf{s}_d = \int_{h^-}^{h^+} \boldsymbol{\sigma}_d \, dz = \int_{h^-}^{h^+} [\mathbf{C}_{dm}(\boldsymbol{\varepsilon}_m + (z - z_0)\boldsymbol{\varepsilon}_b) + \mathbf{C}_{dd} \ \boldsymbol{\varepsilon}_d] \, dz = \int_{h^-}^{h^+} \mathbf{C}_{dd} \ \boldsymbol{\varepsilon}_d \ dz = 2\bar{S}_m l^2 \mathbf{I}_2 \boldsymbol{\varepsilon}_d \tag{18}$$

where:

$$\mathbf{R} = \begin{bmatrix} a_1 & a_2 & 0 & 0 \\ a_2 & a_1 & 0 & 0 \\ 0 & 0 & \bar{\mu}_1 & \bar{\mu}_2 \\ 0 & 0 & \bar{\mu}_2 & \bar{\mu}_1 \end{bmatrix}, \quad \mathbf{I}_2 = \begin{bmatrix} 1 & 0 \\ 0 & 1 \end{bmatrix}, \quad \bar{\mu}_1 = \frac{\mu_1}{2(1+\nu)}, \quad \bar{\mu}_2 = \frac{\mu_2}{2(1+\nu)} \tag{19}$$

The shear part of the stress resultants $\mathbf{s}_s$ is calculated as

$$\mathbf{s}_s = \int_{h^-}^{h^+} \boldsymbol{\sigma}_s \, dz = \alpha_s \int_{h^-}^{h^+} \mathbf{C}_{ss} \, \boldsymbol{\varepsilon}_s dz = \alpha_s \bar{S}_m \mathbf{I}_2 \boldsymbol{\varepsilon}_s \tag{20}$$

using the constitutive matrix $\mathbf{C}_{ss} = \begin{bmatrix} G & 0 \\ 0 & G \end{bmatrix}$ and the shear correction factor $\alpha_s = 5/6$. The obtained constitutive matrix is presented as

$$\begin{bmatrix} N^{11} \\ N^{22} \\ N^{12} \\ N^{21} \\ Q^{1} \\ Q^{2} \\ M^{11} \\ M^{22} \\ M^{12} \\ M^{21} \\ M^{1} \\ M^{2} \end{bmatrix} = \left[\begin{array}{cccccc|cccccc} S_m a_1 & S_m a_2 & 0 & 0 & 0 & 0 & 0 & 0 & 0 & 0 & 0 & 0 \\ S_m a_2 & S_m a_1 & 0 & 0 & 0 & 0 & 0 & 0 & 0 & 0 & 0 & 0 \\ 0 & 0 & \bar{S}_m \mu_1 & \bar{S}_m \mu_2 & 0 & 0 & 0 & 0 & 0 & 0 & 0 & 0 \\ 0 & 0 & \bar{S}_m \mu_2 & \bar{S}_m \mu_1 & 0 & 0 & 0 & 0 & 0 & 0 & 0 & 0 \\ 0 & 0 & 0 & 0 & \bar{S}_m \alpha_S & 0 & 0 & 0 & 0 & 0 & 0 & 0 \\ 0 & 0 & 0 & 0 & 0 & \bar{S}_m \alpha_S & 0 & 0 & 0 & 0 & 0 & 0 \\ \hline 0 & 0 & 0 & 0 & 0 & 0 & S_b a_1 & S_b a_2 & 0 & 0 & 0 & 0 \\ 0 & 0 & 0 & 0 & 0 & 0 & S_b a_2 & S_b a_1 & 0 & 0 & 0 & 0 \\ 0 & 0 & 0 & 0 & 0 & 0 & 0 & 0 & \bar{S}_b \mu_1 & \bar{S}_b \mu_2 & 0 & 0 \\ 0 & 0 & 0 & 0 & 0 & 0 & 0 & 0 & \bar{S}_b \mu_2 & \bar{S}_b \mu_1 & 0 & 0 \\ 0 & 0 & 0 & 0 & 0 & 0 & 0 & 0 & 0 & 0 & 2\bar{S}_m l^2 & 0 \\ 0 & 0 & 0 & 0 & 0 & 0 & 0 & 0 & 0 & 0 & 0 & 2\bar{S}_m l^2 \end{array}\right] \begin{bmatrix} \varepsilon_{11} \\ \varepsilon_{22} \\ \varepsilon_{12} \\ \varepsilon_{21} \\ \varepsilon_{1} \\ \varepsilon_{2} \\ \kappa_{11} \\ \kappa_{22} \\ \kappa_{12} \\ \kappa_{21} \\ \kappa_{1} \\ \kappa_{2} \end{bmatrix} \tag{21}$$

Comparing the value of drilling component of the constitutive matrix in (21) with value from [54] we obtain following equivalent relations

$$\alpha_t D(1-\nu) = 2\bar{S}_m l^2 \quad \Leftrightarrow \quad \alpha_t \frac{Eh^3}{12(1-\nu^2)}(1-\nu) = 2\frac{S_m}{2(1+\nu)} l^2 \tag{22}$$

which provide the identification

$$l = \sqrt{\frac{Eh^3 \alpha_t}{12 S_m}} \quad \Leftrightarrow \quad \alpha_t = 12 \frac{S_m}{Eh} \left(\frac{l}{h}\right)^2 \tag{23}$$

The equations (23) show that the parameter α_t could be interpreted as the material parameter connected with the micropolar length. Hence, influence of l on the results will have similar character under given *N* and *n* as that of α_t for isotropic material, see [54].

4. Results

In all numerical examples we assume the following values of Young's modulus: $E_c = 1.51 \times 10^9$ for the ceramic constituent, $E_m = 0.7 \times 10^9$ for the metal constituent and constant value of Poisson's ratio $\nu = 0.3$. For micropolar material we assume $N = \frac{1}{2}\sqrt{2}$ and various values of the micropolar characteristic length that we determine as the ratio to the shell thickness $\frac{l}{h_0}$. We chose materials characterized by power-law exponent $n = \{0; 0.5; 2.0; 10^6\}$. In

two last examples we assume $n = 2.0$, as the closest integer to $n_{\max} = 2.077$ that gives maximal value of the shift of the neutral physical reference surface.

4.1. Cylinder

We analyze cylindrical shell with free edges which is subjected to two opposite point loads, see Fig. 33. This is quite popular benchmark problem e.g. [8,26,55,56]. On the grounds of the present shell theory this example has been analyzed in [43] using 16-node CAM elements [54] with full integration and middle surface approach. We use the following data: $L = 10.35$, $R = 4.953$, $h_0 = 0.094$, $P_{\text{ref}} = 10^6$, $P = \frac{1}{4}\lambda P_{\text{ref}}$. Triple symmetry of the structure is used with the regular mesh 36×36 of EANS elements. The internal surface of the shell is assumed to be metal rich while the external surface is ceramic rich. The material has variable micropolar characteristic length as the ratio to the shell thickness $\frac{l}{h_0} = \{0.01; 0.1; 1; 10\}$. Obtained load-displacement paths of displacements w_a and $-u_b$ for $\frac{l}{h_0} = 0.01$ are plotted in Fig. 44. Thick solid line in the background for $n = 2.0$ denotes the solution computed with the present element, but with middle surface approach [43]. The obtained results are in good correspondence with the reference solution [8]. It is visible that the curves describe two distinctive behaviors: bending dominated attributed to the flexural stiffness of the shell and tension dominated due to the increasing membrane stiffness. In the first part large displacements are observed, while for $w_a > 2.5$ the greater tension stiffness of the shell substantially reduces further increments of displacements.

The influence of variable $\frac{l}{h_0} = \{0.1; 1; 10\}$ is portrayed in Fig. 5. We observe that for $l = 10h_0$ the shape of the curves changes and characteristic plateau disappears. For each studied *n* it is also visible that with increase of the characteristic length the displacements' values decrease. The displacement components *u* and *w* computed on the *a* – *b* path for $\lambda = 0.5$ are

compared in Fig. 6 for different values of the power-law exponent. The curves show that the shell undergoes the most pronounced deformations when FGM material parameter $n=10^6$. In particular, the difference in horizontal displacement of point *b* amounts to ≈ 1. In Table 1 the comparison of numerical values is presented for selected load levels and different *n* and $\frac{l}{h_0}$.

Analysis of the results indicates that the response of the shell predicted by the middle surface approach is less stiffer in comparison to that obtained using the neutral surface model.

4.2. Hyperboloid shell

Following [57] we consider the well-known example of hyperboloid shell under action of two pairs of opposite point forces. This shell is the popular example especially for laminated shells e.g. [56,58–60]. Quoting Arciniega and Reddy [59] „*This challenging example demonstrates the robustness of the present finite element model and its applicability to arbitrary shell geometries and very strong geometric nonlinearity*". Here we assume functionally graded material. The geometry (see Fig. 7) and load used in the analysis are: $h_0=0.04$, $R_1=7.5$, $R_2=15$, $H=20.0$, $R(y)=R_1\sqrt{1+(y/C)^2}$, $C=20/\sqrt{3}$, $P_{ref}=5$, $P(\lambda)=\lambda P_{ref}$. Due to the symmetry only one eight of the structure is analyzed with 60×60 EANS element mesh. The obtained results for $n=\{0;0.5;2.0;10^6\}$ and the ratio $l=0.01h_0$ are shown as the equilibrium paths in Fig. 8. As in the previous example the thick solid line in the background for $n=2.0$ denotes the solution obtained with middle surface approach. It is noticeable that in the presented scale the curves are indistinguishable. As the influence of ratio $\frac{l}{h_0}$ is relatively small we compare values of characteristic displacements for $l=0.01h_0$ and $l=10h_0$ in Table 2. The data shows that with the growth of volume fraction exponent n, as in the previous example, the shell becomes more flexible which is easy to explain due to change in the material structure from ceramic rich to metal rich. The influence of the characteristic length has the same character as in

the preceding example, i.e. larger values of $\frac{l}{h_0}$ make the structure stiffer. Moreover, the neutral surface model yields smaller values of displacements. Similarly, we present in Fig. 9 displacements *u*, *w* computed at nodes placed on the *a* – *b* path for $y = 0$ and $P = 7500$.

4.3. Hinged spherical shell with concentrated load

Following e.g. [61–63] we analyze the hinged spherical shell with concentrated load, see Fig. 10, with the following data $R = 2.54$, $a = 0.7849$, $h_0 = 0.09945$, $P_{ref} = 1000$, $P = \lambda P_{ref}$. Due to symmetry, only quarter of the shell is analyzed with proper boundary conditions at symmetry planes. Outer edges are hinged, i.e. only one rotational DOF at each of them is free (translations and remaining rotations are fixed). In the cited papers, the shell is treated as isotropic, so that none of them provide reference results for FGM material. In present calculations, quarter of the shell is divided into 24x24 EANS elements. In comparison with previous examples the present shell is relatively thick. Thus, instead of parametric analysis with respect to values of the power-law exponent n and ratio $\frac{l}{h_0}$ we fix them as $n = 2$, $l = 0.01h_0$ and compare the results obtained for neutral and middle surface approaches. We assume three values of the shell thickness: $h = \{h_0, 0.5h_0, 0.25h_0\}$ to evaluate the influence of the shell thickness. As the reference values we use those computed in Abaqus 6.14 (Dassault Systemes Simulia Corp. Providence, USA), with two element types: S4 and S8R, both 24x24 element discretization. FGM constitutive relation in Abaqus was implemented through our own Python script and the generalized shell section feature.

The obtained equilibrium paths are shown in Fig. 11. Analysis was conducted with displacement control algorithm. This example exhibits a typical snap-through phenomenon. The overall shape of equilibrium path is similar to that obtained in isotropic material analyses [61–63], with two snap-trough points. Discrepancy between neutral and middle surface approach is clearly visible in the results obtained from either FEM code. In contrast to the previous examples, the neutral surface approach gives less stiff shell deformation for λ lower than

critical buckling value. It is also noticeable that the higher order shell elements S8R provide the results more consistent with EANS approach. Fig. 12 shows the influence of the shell thickness. The reduction of the shell thickness causes the drop of load multiplier λ value for fixed control displacement w_c. We observe also that the relative difference between the neutral and middle surface approaches diminishes with reduction of the thickness (Table 3).

4.4. Box section column under compression

This example demonstrates the capability of the present shell theory and finite elements to deal with geometry with orthogonal intersections. Compression of the column with rectangular cross-section and the following geometric dimensions: $a=1.0$, $b=0.5$, $L=2.0$, h_0=0.05 is analyzed, see Fig. 13. We assume the regular discretization (30 + 15 + 30 + 15)×60 of EANS elements in nonlinear analysis. The compression forces *P* are applied in four corners of box section with reference value $P_{ref}=2.5\cdot10^5$, $P=\lambda P_{ref}$. Additionally, the constraint enforcing the constant value of displacement *v* at each node on the top edges of the column is introduced. Only translational DOFs are constrained at two ends of the FGM box (Fig. 13). The uniform compression of the square box sigmoid FGM section was analyzed in paper [9].

In this example, similar as for hinged spherical shell, we compare the results obtained with the neutral and middle surface approaches. Hence, the constant value of the power-law exponent $n=2.0$ and values of micropolar parameters N=0.707, l/h_0=0.01 are assumed in analyses. The box column deformation shapes for the neutral and middle surface approaches are presented in Fig. 14 on contour maps of displacement *u* for the specified load level $\lambda=1.5$. The shapes of box wall deformation in the xy symmetry plane for three different levels of load are depicted in Fig. 15. The curves of horizontal displacement *u* and vertical displacement *v* at the point A (Fig. 13) as function of load multiplier λ ($F=4P=4\lambda P_{ref}=\lambda\cdot10^6$) are presented in Fig. 16. The box section deformation before buckling is significantly smaller for the neutral surface approach. In consequence, we observe buckling of the column for smaller value of λ in middle surface approach.

5. Conclusions

We have analyzed the behavior of FGM shells with drilling rotation under combined influence of the FGM constants and micropolar material parameters. Definition of EANS shell element with respect to the neutral reference surface has been presented. The equilibrium paths obtained for the cylindrical shell are consistent with paths from [8]. The influence of the micropolar characteristic length on the nonlinear response of FGM shells is close to that for homogenous shells. We observe for $l/h_0 > 10$ significantly stiffer behavior of the FGM structures. The nonlinear curves for FGM section are located between the curves for metal and ceramic shell.

In the middle surface formulation the external force is applied eccentrically with respect to the physical neutral surface. Hence, we have observed earlier buckling in case of middle surface approach and greater stiffness of FGM shells calculated with neutral surface formulation. Only exception is the example of hinged spherical shell that we explain by snap-through phenomenon. The difference between these two approaches is visible especially in the nonlinear range for relatively thick shells and is proportional to the shift of the neutral physical surface. The shift depends on shell thickness, the power-law exponent and ratio of the ceramic and metal elastic moduli. In the parametric analysis we have observed that relative difference between these two approaches is almost proportional to shell thickness.

Acknowledgements

The research reported in this paper was supported by the National Science Centre, Poland with the grant UMO-2015/17/B/ST8/02190. Abaqus calculations were carried out at the Academic Computer Centre in Gdańsk.

References

[1] Koizumi M. FGM activities in Japan. Compos Part B Eng 1997;28:1–4.

doi:10.1016/S1359-8368(96)00016-9.

[2] Swaminathan K, Naveenkumar DT, Zenkour AM, Carrera E. Stress, vibration and buckling analyses of FGM plates—A state-of-the-art review. Compos Struct 2015;120:10–31. doi:10.1016/j.compstruct.2014.09.070.

[3] Woo J, Meguid SA. Nonlinear analysis of functionally graded plates and shallow shells. Int J Solids Struct 2001;38:7409–21. doi:10.1016/S0020-7683(01)00048-8.

[4] Ghannadpour SAM, Alinia MM. Large deflection behavior of functionally graded plates under pressure loads. Compos Struct 2006;75:67–71. doi:10.1016/j.compstruct.2006.04.004.

[5] Chi S-H, Chung Y-L. Mechanical behavior of functionally graded material plates under transverse load—Part II: Numerical results. Int J Solids Struct 2006;43:3675–91. doi:10.1016/j.ijsolstr.2005.04.010.

[6] Yang J, Shen H-S. Non-linear analysis of functionally graded plates under transverse and in-plane loads. Int J Non Linear Mech 2003;38:467–82. doi:10.1016/S0020-7462(01)00070-1.

[7] Ma LS, Wang TJ. Nonlinear bending and post-buckling of a functionally graded circular plate under mechanical and thermal loadings. Int J Solids Struct 2003;40:3311–30. doi:10.1016/S0020-7683(03)00118-5.

[8] Arciniega RA, Reddy JN. Large deformation analysis of functionally graded shells. Int J Solids Struct 2007;44:2036–52. doi:10.1016/j.ijsolstr.2006.08.035.

[9] Han SC, Lee WH, Park WT. Non-linear analysis of laminated composite and sigmoid functionally graded anisotropic structures using a higher-order shear deformable natural Lagrangian shell element. Compos Struct 2009;89:8–19. doi:10.1016/j.compstruct.2008.08.006.

[10] Viola E, Rossetti L, Fantuzzi N, Tornabene F. Static analysis of functionally graded conical shells and panels using the generalized unconstrained third order theory coupled with the stress recovery. Compos Struct 2014;112:44–65. doi:10.1016/j.compstruct.2014.01.039.

[11] Fazzolari FA. Stability analysis of FGM sandwich plates by using variable-kinematics Ritz models. Mech Adv Mater Struct 2016;23:1104–13.

doi:10.1080/15376494.2015.1121559.

[12] Taczała M, Buczkowski R, Kleiber M. Postbuckling analysis of functionally graded plates on an elastic foundation. Compos Struct 2015;132:842–7. doi:10.1016/j.compstruct.2015.06.055.

[13] Tornabene F, Reddy JN. FGM and laminated doubly-curved and degenerate shells resting on nonlinear elastic foundations: A GDQ solution for static analysis with a posteriori stress and strain recovery. J Indian Inst Sci 2013;93:635–88.

[14] Fazzolari FA, Carrera E. Refined hierarchical kinematics quasi-3D Ritz models for free vibration analysis of doubly curved FGM shells and sandwich shells with FGM core. J Sound Vib 2014;333:1485–508. doi:10.1016/j.jsv.2013.10.030.

[15] Tornabene F, Fantuzzi N, Bacciocchi M, Viola E. Effect of agglomeration on the natural frequencies of functionally graded carbon nanotube-reinforced laminated composite doubly-curved shells. Compos Part B Eng 2016;89:187–218. doi:10.1016/j.compositesb.2015.11.016.

[16] Fazzolari FA. Reissner's Mixed Variational Theorem and variable kinematics in the modelling of laminated composite and FGM doubly-curved shells. Compos Part B Eng 2016;89:408–23. doi:10.1016/j.compositesb.2015.11.031.

[17] Tornabene F, Fantuzzi N, Bacciocchi M. Free vibrations of free-form doubly-curved shells made of functionally graded materials using higher-order equivalent single layer theories. Compos Part B Eng 2014;67:490–509. doi:10.1016/j.compositesb.2014.08.012.

[18] Fazzolari FA. Natural frequencies and critical temperatures of functionally graded sandwich plates subjected to uniform and non-uniform temperature distributions. Compos Struct 2015;121:197–210. doi:10.1016/j.compstruct.2014.10.039.

[19] Fantuzzi N, Tornabene F, Viola E. Four-parameter functionally graded cracked plates of arbitrary shape: A GDQFEM solution for free vibrations. Mech Adv Mater Struct 2016;23:89–107. doi:10.1080/15376494.2014.933992.

[20] Fazzolari FA, Carrera E. Coupled thermoelastic effect in free vibration analysis of anisotropic multilayered plates and FGM plates by using a variable-kinematics Ritz formulation. Eur J Mech A/Solids 2014;44:157–74. doi:10.1016/j.euromechsol.2013.10.011.

[21] Morimoto T, Tanigawa Y, Kawamura R. Thermal buckling of functionally graded rectangular plates subjected to partial heating. Int J Mech Sci 2006;48:926–37. doi:10.1016/j.ijmecsci.2006.03.015.

[22] Abrate S. Functionally graded plates behave like homogeneous plates. Compos Part B Eng 2008;39:151–8. doi:10.1016/j.compositesb.2007.02.026.

[23] Zhang DG, Zhou YH. A theoretical analysis of FGM thin plates based on physical neutral surface. Comput Mater Sci 2008;44:716–20. doi:10.1016/j.commatsci.2008.05.016.

[24] Prakash T, Singha MK, Ganapathi M. Influence of neutral surface position on the nonlinear stability behavior of functionally graded plates. Comput Mech 2009;43:341–50. doi:10.1007/s00466-008-0309-8.

[25] Kugler S, Fotiu PA, Murin J. The numerical analysis of FGM shells with enhanced finite elements. Eng Struct 2013;49:920–35. doi:10.1016/j.engstruct.2012.12.033.

[26] Witkowski W. 4-node combined shell element with semi-EAS-ANS strain interpolations in 6-parameter shell theories with drilling degrees of freedom. Comput Mech 2009;43:307–19. doi:10.1007/s00466-008-0307-x.

[27] Simo JC, Rifai MS. A class of mixed assumed strain methods and the method of incompatible modes. Int J Numer Methods Eng 1990;29:1595–638. doi:10.1002/nme.1620290802.

[28] Bathe K-J, Dvorkin EN. A formulation of general shell elements—the use of mixed interpolation of tensorial components. Int J Numer Methods Eng 1986;22:697–722. doi:10.1002/nme.1620220312.

[29] Areias P, Rabczuk T, César De Sá JM, Garção JE. Finite strain quadrilateral shell using least-squares fit of relative Lagrangian in-plane strains. Finite Elem Anal Des 2015;98:26–40. doi:10.1016/j.finel.2015.01.004.

[30] Areias P, Rabczuk T, César De Sá JM, Natal Jorge R. A semi-implicit finite strain shell algorithm using in-plane strains based on least-squares. Comput Mech 2015;55:673–96. doi:10.1007/s00466-015-1130-9.

[31] Ivannikov V, Tiago C, Pimenta PM. Generalization of the C1 TUBA plate finite elements to the geometrically exact Kirchhoff–Love shell model. Comput Methods Appl

Mech Eng 2015;294:210–44. doi:10.1016/j.cma.2015.05.018.

[32] Reissner E. Linear and nonlinear theory of shells. In: Fung YC, Sechler EE, editors. Thin Shell Struct., Englewood Cliffs: Prentice-Hall; 1974, p. 29–44.

[33] Libai A, Simmonds JG. The Nonlinear Theory of Elastic Shells. 2nd ed. Cambridge: Cambridge University Press; 1998.

[34] Pietraszkiewicz W, Konopińska V. Drilling couples and refined constitutive equations in the resultant geometrically non-linear theory of elastic shells. Int J Solids Struct 2014;51:2133–43. doi:10.1016/j.ijsolstr.2014.02.022.

[35] Eremeyev VA, Lebedev LP. Existence theorems in the linear theory of micropolar shells. ZAMM Zeitschrift fur Angew Math und Mech 2011;91:468–76. doi:10.1002/zamm.201000204.

[36] Eremeyev VA, Lebedev LP, Cloud MJ. The Rayleigh and Courant variational principles in the six-parameter shell theory. Math Mech Solids 2015;20:806–22. doi:10.1177/1081286514553369.

[37] Birsan M, Neff P. Existence of minimizers in the geometrically non-linear 6-parameter resultant shell theory with drilling rotations. Math Mech Solids 19(4), 2014, 376-397. doi:10.1177/1081286512466659.

[38] Bîrsan M, Neff P. Existence Theorems in the Geometrically Non-linear 6-Parameter Theory of Elastic Plates. J Elast 2013;112:185–98. doi:10.1007/s10659-012-9405-2.

[39] Chróścielewski J, Sabik A, Sobczyk B, Witkowski W. Nonlinear FEM 2D failure onset prediction of composite shells based on 6-parameter shell theory. Thin-Walled Struct 2016;105:207–19. doi:10.1016/j.tws.2016.03.024.

[40] Burzyński S, Chróścielewski J, Witkowski W. Elastoplastic law of Cosserat type in shell theory with drilling rotation. Math Mech Solids 2015;20:790–805. doi:10.1177/1081286514554351.

[41] Burzyński S, Chróścielewski J, Witkowski W. Geometrically nonlinear FEM analysis of 6-parameter resultant shell theory based on 2-D Cosserat constitutive model. ZAMM Zeitschrift fur Angew Math und Mech 2016;96:191–204. doi:10.1002/zamm.201400092.

[42] Nowacki W. Couple-stresses in the theory of thermoelasticity. In: Parkus H, Sedov LI,

editors. Irreversible Asp. Contin. Mech. Transf. Phys. Charact. Mov. fluids. IUTAM Symp. Vienna 1966, Wien: Springer-Verlag; 1968, p. 259–78.

[43] Daszkiewicz K, Chróścielewski J, Witkowski W. Geometrically Nonlinear Analysis of Functionally Graded Shells Based on 2-D Cosserat Constitutive Model. Eng Trans 2014;62:109–30.

[44] Chróścielewski J, Witkowski W. Four-node semi-EAS element in six-field nonlinear theory of shells. Int J Numer Methods Eng 2006;68:1137–79. doi:10.1002/nme.1740.

[45] Chróścielewski J, Witkowski W. Discrepancies of energy values in dynamics of three intersecting plates. Int J Numer Method Biomed Eng 2010;26:1188–202. doi:10.1002/cnm.1208.

[46] Chróścielewski J, Kreja I, Sabik A, Witkowski W. Modeling of Composite Shells in 6–Parameter Nonlinear Theory with Drilling Degree of Freedom. Mech Adv Mater Struct 2011;18:403–19. doi:10.1080/15376494.2010.524972.

[47] Chróścielewski J, Makowski J, Pietraszkiewicz W. Statics and Dynamics of Multi-Shells: Nonlinear Theory and Finite Element Method (in Polish). IFTR PASci Press, Warsaw, 2004.

[48] Pietraszkiewicz W, Eremeyev VA. On vectorially parameterized natural strain measures of the non-linear Cosserat continuum. Int J Solids Struct 2009;46:2477–80. doi:10.1016/j.ijsolstr.2009.01.030.

[49] Ibrahimbegovic A. On the choice of finite rotation parameters. Comput Methods Appl Mech Eng 1997;149:49–71. doi:10.1016/S0045-7825(97)00059-5.

[50] Koay CG. On the six-dimensional orthogonal tensor representation of the rotation in three dimensions: A simplified approach. Mech Mater 2009;41:951–3. doi:10.1016/j.mechmat.2008.12.006.

[51] Khabbaz RS, Manshadi BD, Abedian A. Nonlinear analysis of FGM plates under pressure loads using the higher-order shear deformation theories. Compos Struct 2009;89:333–44. doi:10.1016/j.compstruct.2008.06.009.

[52] Jeong J, Ramezani H, Münch I, Neff P. A numerical study for linear isotropic Cosserat elasticity with conformally invariant curvature. ZAMM Zeitschrift Fur Angew Math Und Mech 2009;89:552–69. doi:10.1002/zamm.200800218.

[53] Hassanpour S, Heppler GR. Micropolar elasticity theory: a survey of linear isotropic equations, representative notations, and experimental investigations. Math Mech Solids 2015:1–19. doi:10.1177/1081286515581183.

[54] Chróścielewski J, Makowski J, Stumpf H. Genuinely resultant shell finite elements accounting for geometric and material non-linearity. Int J Numer Methods Eng 1992;35:63–94. doi:10.1002/nme.1620350105.

[55] Kreja I, Schmidt R. Large rotations in first-order shear deformation FE analysis of laminated shells. Int J Non Linear Mech 2006;41:101–23. doi:10.1016/j.ijnonlinmec.2005.06.009.

[56] Wiśniewski K. Finite rotation shells. Springer; 2010. doi:10.1007/978-90-481-8761-4.

[57] Başar Y, Ding Y, Schultz R. Refined shear-deformation models for composite laminates with finite rotations. Int J Solids Struct 1993;30:2611–38. doi:10.1016/0020-7683(93)90102-D.

[58] Gruttmann F, Wagner W. Structural analysis of composite laminates using a mixed hybrid shell element. Comput Mech 2006;37:479–97. doi:10.1007/s00466-005-0730-1.

[59] Arciniega RA, Reddy JN. Tensor-based finite element formulation for geometrically nonlinear analysis of shell structures. Comput Methods Appl Mech Eng 2007;196:1048–73. doi:10.1016/j.cma.2006.08.014.

[60] Vu-Quoc L, Tan XG. Optimal solid shells for non-linear analyses of multilayer composites. I. Statics. Comput Methods Appl Mech Eng 2003;192:975–1016. doi:10.1016/S0045-7825(02)00435-8.

[61] Horrigmoe G, Bergan PG. Nonlinear analysis of free-form shells by flat finite elements. Comput Methods Appl Mech Eng 1978;16:11–35. doi:10.1016/0045-7825(78)90030-0.

[62] Samanta A, Mukhopadhyay M. Finite element large deflection static analysis of shallow and deep stiffened shells. Finite Elem Anal Des 1999;33:187–208. doi:10.1016/S0168-874X(99)00022-0.

[63] Bathe K-J, Ho L-W. A simple and effective element for analysis of general shell structures. Comput Struct 1981;13:673–81. doi:10.1016/0045-7949(81)90029-8.

Table 1. Representative values of displacements for the cylindrical shell, in brackets values for the middle surface approach are reported

		$n=0.5$		$n=2.0$	
		$l=0.01h_0$	$l=10h_0$	$l=0.01h_0$	$l=10h_0$
$P=12.5\times10^3$	w_a	0.43512 (0.43579)	0.42857 (0.42923)	0.514493 (0.515740)	0.506826 (0.508067)
	$-u_b$	0.42150 (0.42219)	0.41949 (0.42018)	0.506660 (0.507971)	0.504369 (0.505671)
$P=50\times10^3$	w_a	1.18416 (1.18579)	1.16845 (1.17007)	1.31735 (1.32017)	1.29986 (1.30268)
	$-u_b$	1.35781 (1.35987)	1.35456 (1.35660)	1.55731 (1.56100)	1.55459 (1.55827)
$P=100\times10^3$	w_a	1.63584 (1.63791)	1.61418 (1.61626)	1.75699 (1.76047)	1.73327 (1.73675)
	$-u_b$	2.08847 (2.09142)	2.08884 (2.09177)	2.30399 (2.30909)	2.30752 (2.31259)

Table 2. Representative values of displacements for the hyperboloid shell, in brackets values for the middle surface approach are reported

		$n=0.5$		$n=2$	
		$l=0.01h_0$	$l=10h_0$	$l=0.01h_0$	$l=10h_0$
$P=1500$	$-w_a$	1.87077 (1.87140)	1.86733 (1.86797)	2.12633 (2.12746)	2.12204 (2.12316)
	u_b	1.69661 (1.69720)	1.69452 (1.69511)	1.89137 (1.89239)	1.88860 (1.88962)
$P=3000$	$-w_a$	2.80523 (2.80610)	2.79850 (2.79936)	3.09669 (3.09818)	3.08885 (3.09033)
	u_b	2.35659 (2.35734)	2.35146 (2.35221)	2.53389 (2.53517)	2.52763 (2.52890)
$P=4500$	$-w_a$	3.40122 (3.40221)	3.39221 (3.39319)	3.70207 (3.70373)	3.69147 (3.69312)
	u_b	2.70603 (2.70686)	2.69863 (2.69945)	2.86519 (2.86657)	2.85661 (2.85799)
$P=6000$	$-w_a$	3.83178 (3.83284)	3.82048 (3.82153)	4.12967 (4.13144)	4.11628 (4.11802)
	u_b	2.93011 (2.93099)	2.92105 (2.92192)	3.07453 (3.07597)	3.06431 (3.06575)

Table 3. Influence of the shell thickness on difference between the middle and neutral surface approaches – limit loads comparison.

		Middle surface	Neutral surface	λ % change
$h=h_0$	λ, $-w_c$	71.9561, 0.171	67.6377, 0.157	–6.0
$h=\frac{1}{2}h_0$	λ, $-w_c$	14.0089, 0.190	13.5944, 0.182	–3.0
$h=\frac{1}{4}h_0$	λ, $-w_c$	3.08093, 0.204	3.04107, 0.205	–1.3

Figure captions

Fig. 1. Kinematics of the shell in 6-parameter theory

Fig. 2. FGM shell section, neutral surface position

Fig. 3. Cylindrical shell, geometry and loads

Fig. 4. Cylindrical shell, comparison with reference solution [8]

Fig. 5. Cylindrical shell, neutral surface approach, influence of $\frac{l}{h_0}$ and n on the equilibrium paths

Fig. 6. Cylindrical shell, values of displacements on the XZ symmetry plane, $\lambda = 0.5$, the neutral surface approach

Fig. 7. Hyperboloid shell, geometry and loads

Fig. 8. Hyperboloid shell, influence of the power-law exponent on the equilibrium paths

Fig. 9. Hyperboloid shell, the neutral surface approach, values of displacements u, w on the symmetry plane XZ, $\lambda = 1500$

Fig. 10. Hinged spherical shell, geometry and load

Fig. 11. Hinged spherical shell, comparison of equilibrium paths for EANS element with those for: a) Abaqus S4 element, b) Abaqus S8R element, assumed parameters: $n = 2.0$, $l = 0.01 h_0$, $N = \frac{1}{2}\sqrt{2}$

Fig. 12. Hinged spherical shell, influence of shell thickness on the equilibrium paths

Fig. 13. Box section column under compression, geometry and loads

Fig. 14. Contour of box column displacements u for: a) neutral physical surface approach, b) middle surface approach ($\lambda = 1.5$)

Fig. 15. Comparison of shell deformation in vertical cross section through node A between neutral and middle surface formulations

Fig. 16. Equilibrium paths of displacements u, v in node A, computed with neutral and middle surface approaches

Figure 1

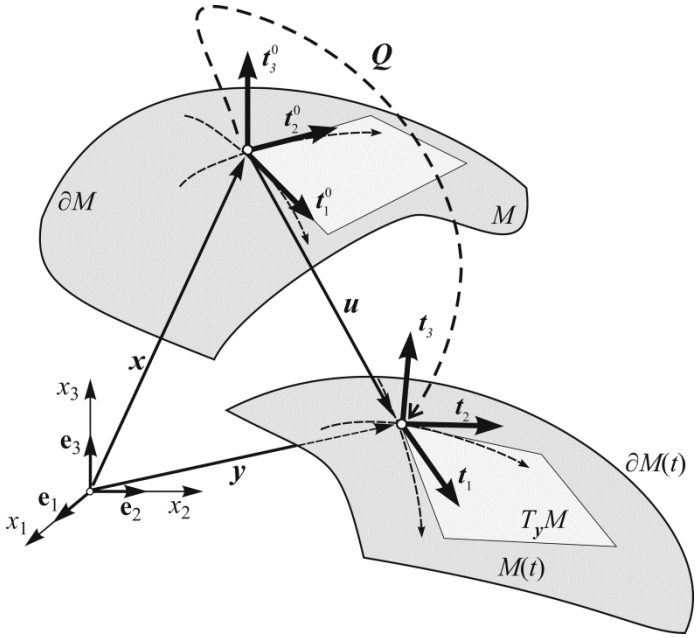

Figure 2

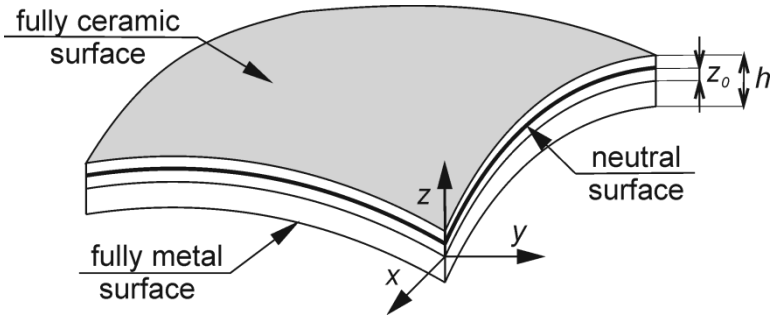

Figure 3

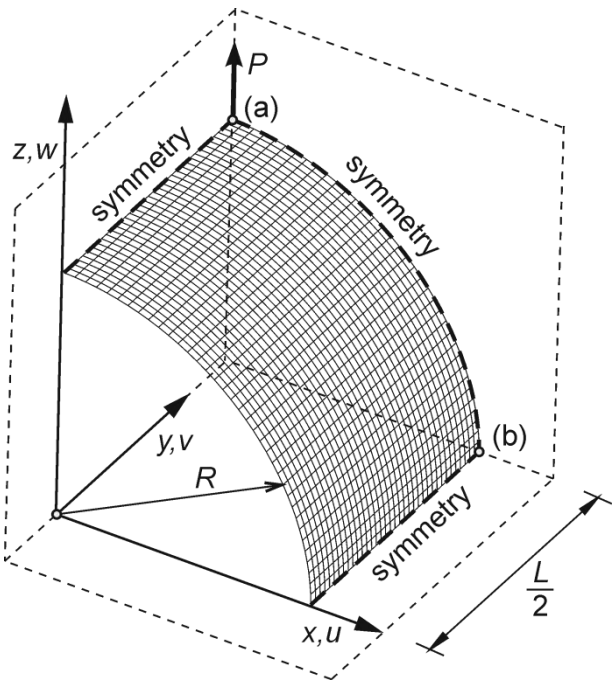

Figure 4

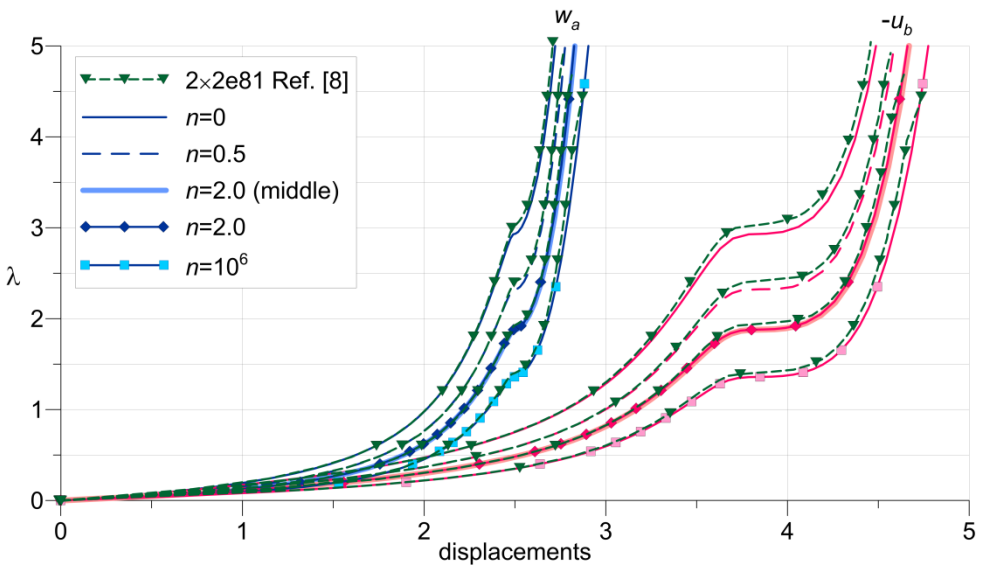

Figure 5

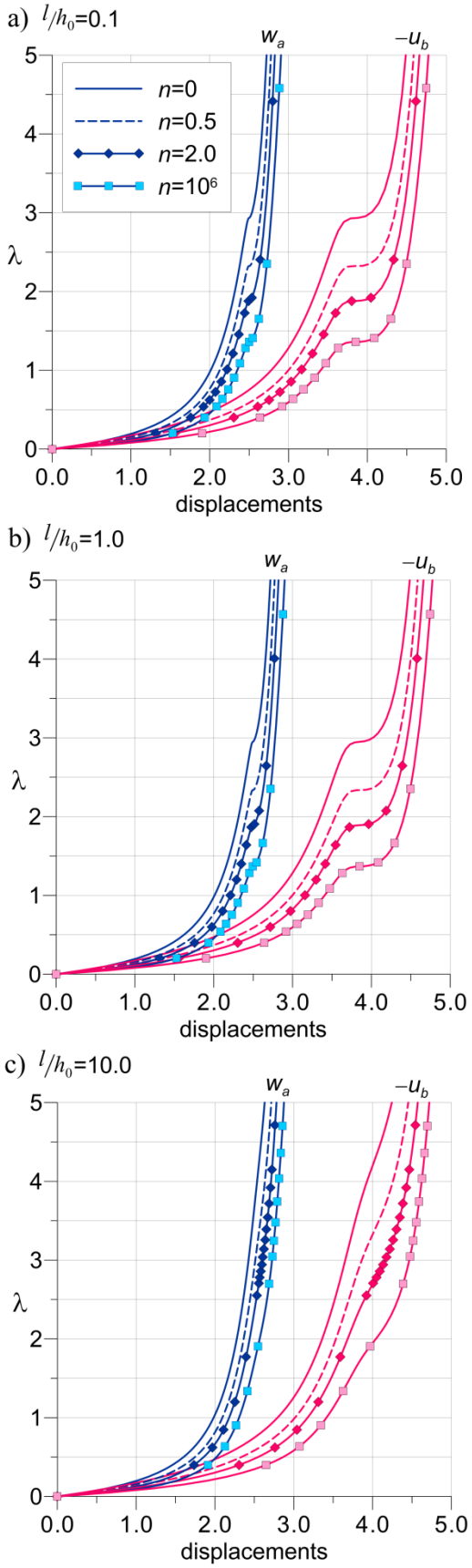

Figure 6

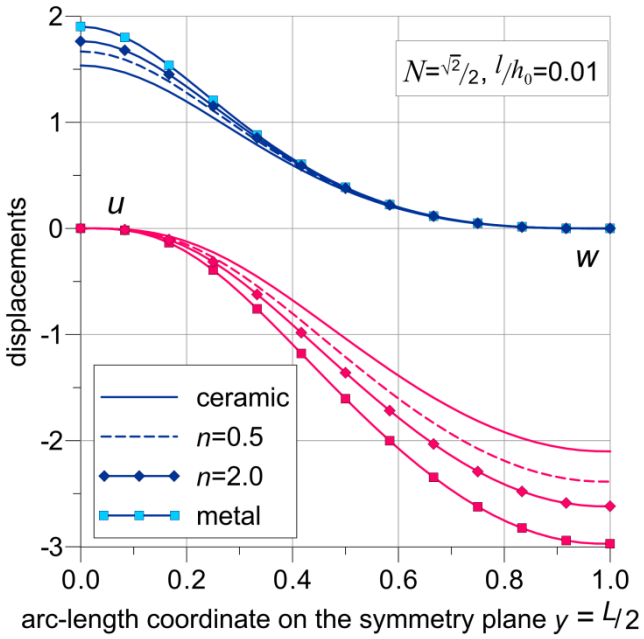

Figure 7

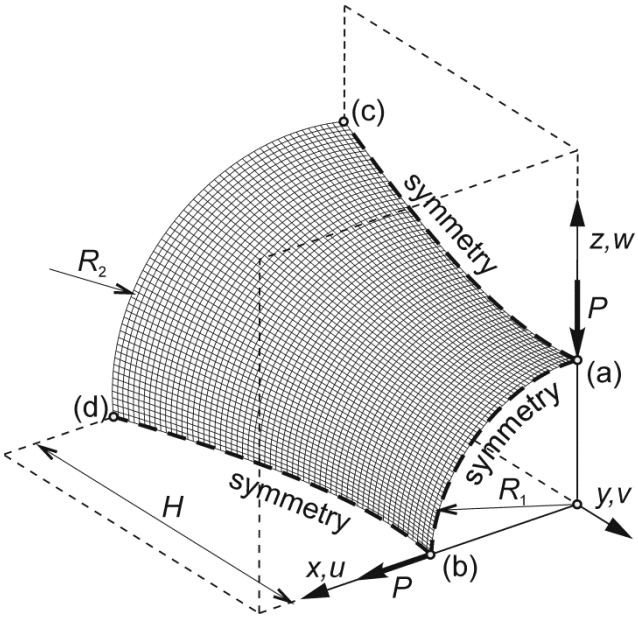

Figure 8

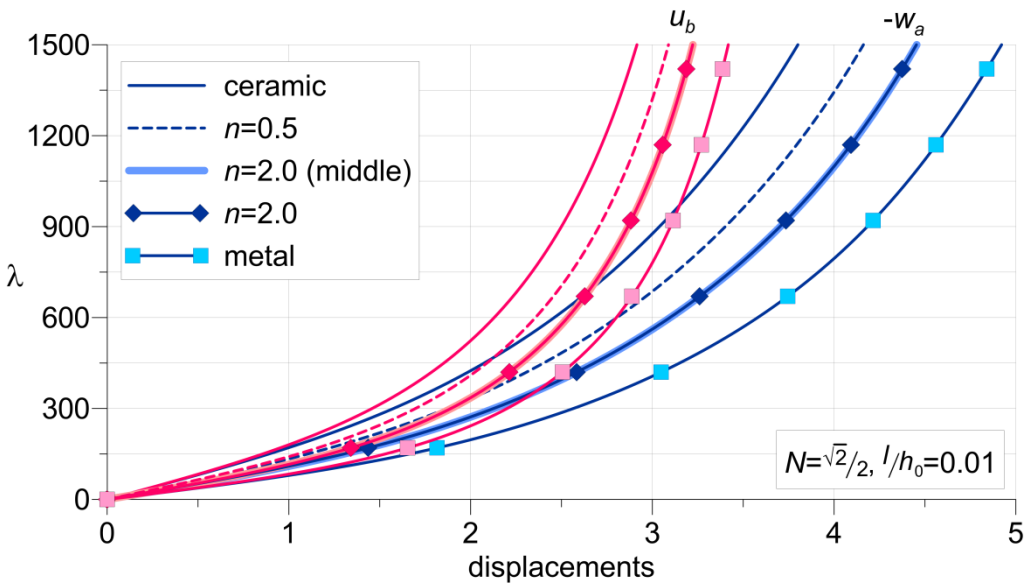

Figure 9

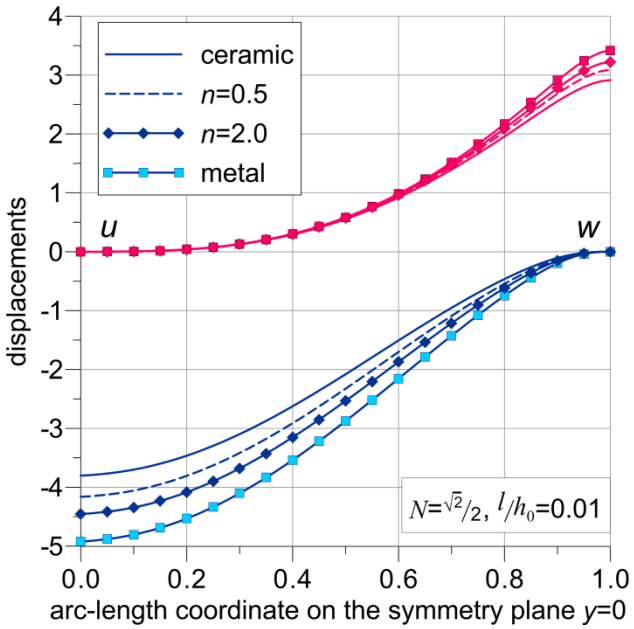

Figure 10

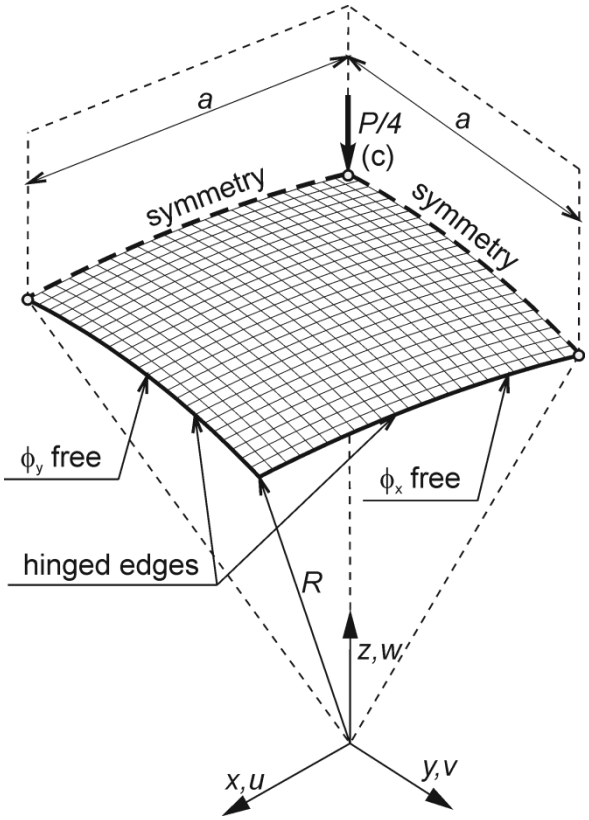

Figure 11

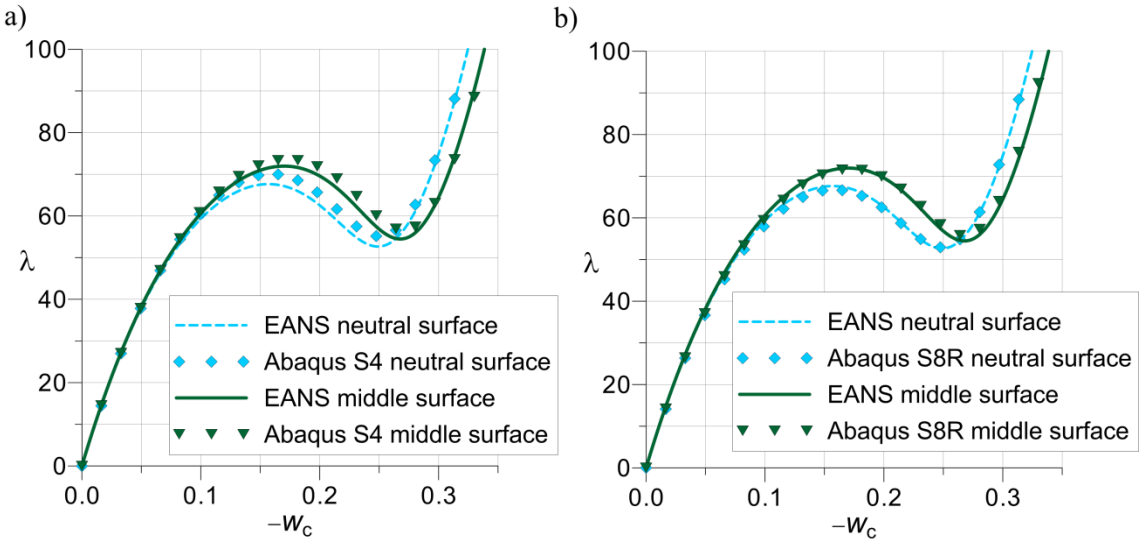

Figure 12

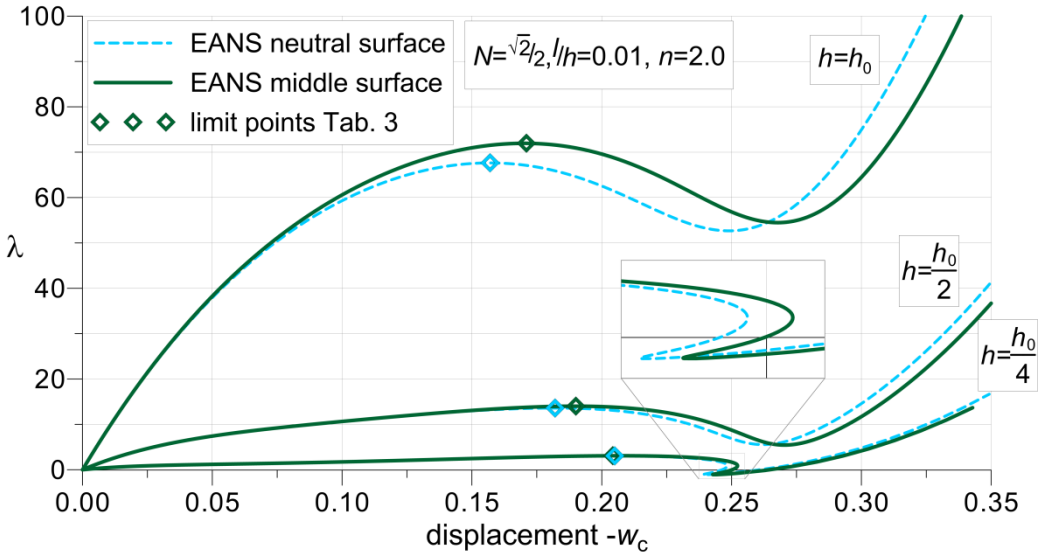

Figure 13

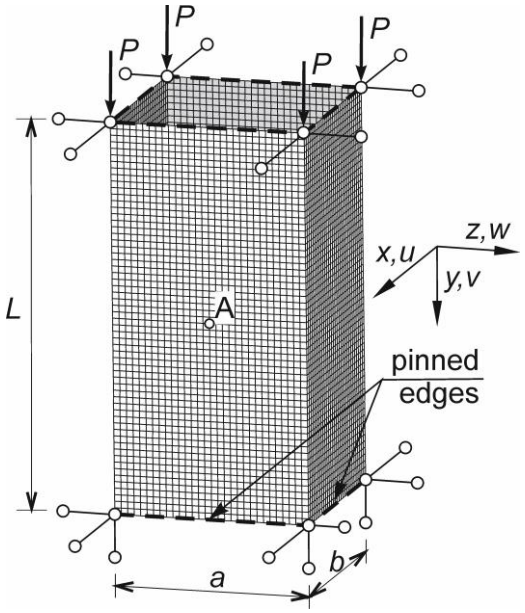

Figure 14

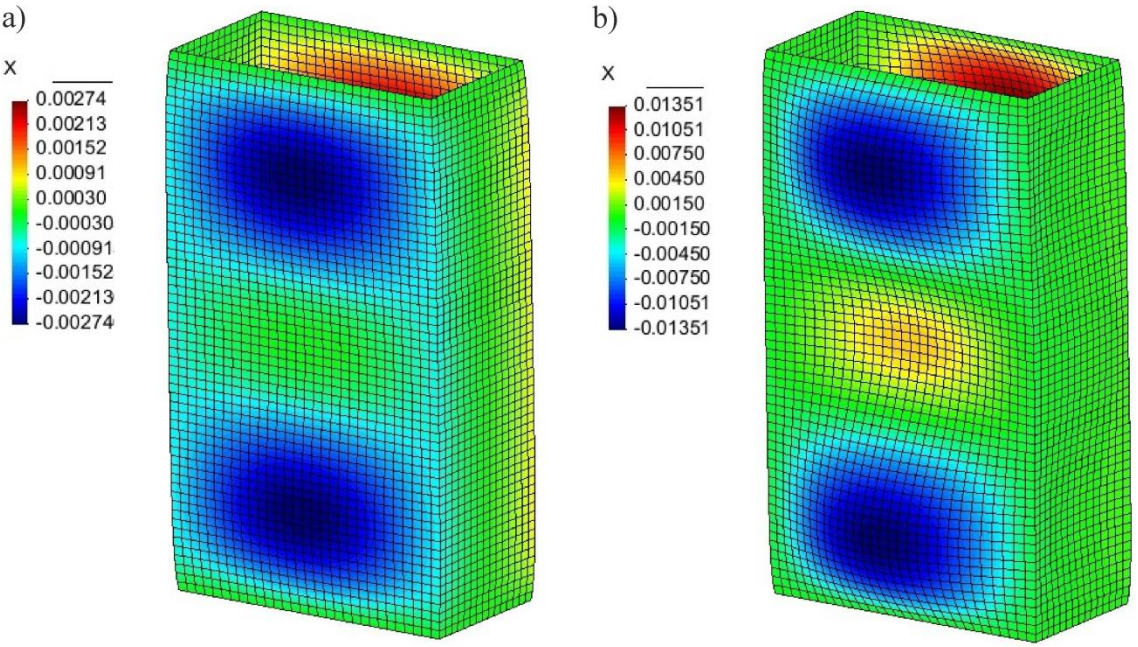

Figure 15

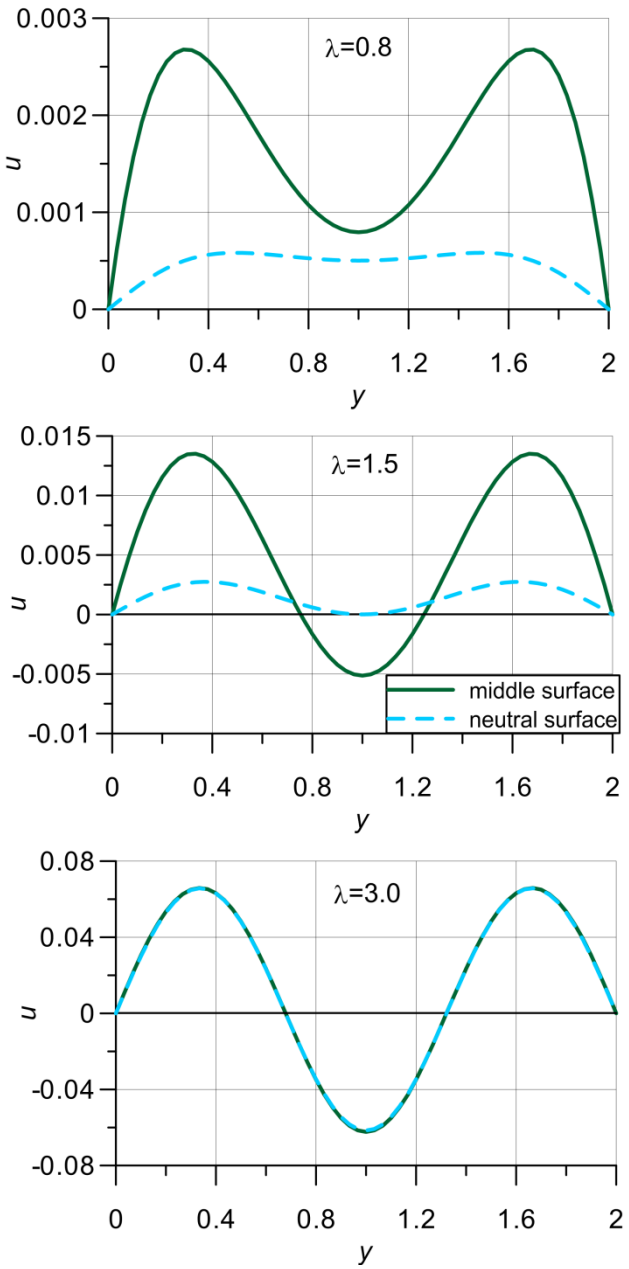

Figure 16